Electrochimica Acta 492 (2024) 144353

Contents lists available at ScienceDirect

Electrochimica Acta

journal homepage: www.journals.elsevier.com/electrochimica-acta

Oxygen reduction reaction platinum group metal-free electrocatalysts derived from spent coffee grounds

Giovanni Zuccante [a,b], Maurizio Acciarri [a], Carmelo Lo Vecchio [c], Irene Gatto [c], Vincenzo Baglio [c], Nicolò Pianta [a], Riccardo Ruffo [a], Luciano Navarini [d], Carlo Santoro [a,*]

[a] Electrocatalysis and Bioelectrocatalysis Lab, Department of Materials Science, University of Milano-Bicocca, U5, Via Cozzi 5, Milano 20125, Italy
[b] Department of Industrial Engineering, University of Padova, Via Marzolo 9, Padova 35131, Italy
[c] Institute for Advanced Energy Technologies "Nicola Giordano" CNR-ITAE, Via Salita S. Lucia sopra Contesse 5, Messina 98126, Italy
[d] illycaffè S.p.A., Via Flavia 110, Trieste 34147, Italy

ARTICLE INFO

Keywords:
Oxygen reduction reaction
Alkaline media
Platinum group metal-free electrocatalysts
Spent coffee grounds
Circular economy

ABSTRACT

The annual generation of coffee waste has overtaken 6 million metric tons, becoming a serious environmental problem. Herein, we report the fabrication of bimetallic electrocatalysts synthesized by 1) pyrolyzing spent coffee grounds (SCGs) at 400, 600, 800 and 1000 °C, 2) activating the as-obtained char with KOH and 3) functionalizing the activated carbon with iron(II) and manganese(II) phthalocyanine. The final electrocatalysts showed a high degree of amorphousness, defectivity (increasing with temperature) and high specific surface area (up to 1820 $m^2 g^{-1}$). In half-cell compartment (0.1 M KOH electrolyte), the top-notch material in terms of oxygen reduction reaction (ORR) activity and selectivity was CFeMn_600, which showed the same half-wave potential ($E_{1/2}$) compared to Pt/C standard along with a lower peroxide production. These outstanding results could be attributed to a high surface area, a Fe-Mn synergy, and an abundance of C-N defects. The performance of CFeMn_600 as a cathode material in alkaline exchange membrane fuel cells (AEMFC) showed an open circuit voltage (OCV) of 0.890 V and power density of 30 mW cm^{-2}. Notwithstanding, this research is one of few cases where a waste-derived electrocatalyst is tested in a real AEMFC, thus becoming a pioneer in the fuel cell study of waste-derived electrode materials.

1. Introduction

The consequences of the carbon emission associated with the excessive consumption of fossil fuels call for new avenues in the global energy supply. Fuel cell (FC) technology is emerging as a valid means to support the production of green energy from hydrogen since FCs exhibit high energy conversion efficiency, modular design, rapid load response and low chemical and acoustical pollution [1,2]. Among the different types of FCs, low-temperature FCs are gaining great attention due to their advantages compared to their high-temperature counterparts, which are mainly limited by the slow on/off process [3–6]. In the paramount of low-temperature FCs, alkaline anion exchange membrane fuel cells (AEMFCs) are devices that can attain high power densities and quite a long lifespan [7–9]. Although AEMFCs are experiencing noticeable success in the market of green technology, the sluggish kinetics of oxygen reduction reaction (ORR) compared to that of hydrogen oxidation reaction (HOR) still represents one of the main bottlenecks of AEMFCs working, which impedes their widespread commercialization [10]. ORR can essentially follow either a two-electron transfer or a four-electron pathway. The former gives rise to hydrogen peroxide (H_2O_2) in acid or peroxide ion HO_2^- (in alkaline) while the latter produces H_2O in acid or OH^- in alkaline [11]. Additionally, an indirect electron transfer, known as a 2 × 2-electron pathway, can take place during the ORR mechanism [12]. In this case, oxygen is firstly reduced to peroxide at higher cathodic potentials and this intermediate is subsequently reduced to H_2O or OH^- at lower cathodic potentials [13–16]. Pursuing a four-electron pathway is of paramount importance to guarantee the correct functioning of the device since the peroxide species can severely damage the membrane integrated into the fuel cell system [11, 17].

To face the aforementioned issues, platinum is usually nanodispersed on carbon supports within the cathodic catalyst layer to boost ORR [18, 19]. However, the high price and scarcity of this raw material renders the application of fuel cells less competitive than the current fossil

* Corresponding author.
E-mail address: carlo.santoro@unimib.it (C. Santoro).

https://doi.org/10.1016/j.electacta.2024.144353
Received 21 December 2023; Received in revised form 18 April 2024; Accepted 27 April 2024
Available online 28 April 2024

fuel-based technology. The usage of Pt for boosting ORR kinetics accounts for more than 50 % of the stack cost [20]. The scientific community has made strong efforts to find possible alternatives, known as platinum metal group-free (PGM-free) electrocatalysts [14,21–23]. Among them, TM-N-C single-site electrocatalysts containing earth-abundant transition metals (TMs) like Fe, Mn, Co, Ni, etc. have withdrawn the attention of scientists due to their low cost compared to PGMs and comparable activity in AEMFCs, where the higher ORR kinetics and less corrosive electrolyte make the PGMs substitution more feasible than in fuel cell working in acidic environment [22,24–26]. From the structural point of view, the main active sites of MNCs are represented by MN_x, where the metallic center is coordinated by x pyridinic nitrogen ligands ($x = 2,3,4$) on a defective carbon surface, thus bio-mimicking the enzymatic active sites for O_2 reduction [12,27].

Many synthetic ways of TM-N_x-Cs production have been explored so far by mixing metal salts with organic precursors of nitrogen and carbon or by harnessing M-N_4 metallic macrocyclic compounds such as metal phthalocyanines, porphyrins, and tetraazannulenes [28–33]. The metal center of these compounds could promote the cleavage of O=O and the subsequent reduction of oxygen, but the M-N_4 macrocycles suffer from poor stability, low electronic conductivities, and environment-limited activities [28]. Therefore, a heat treatment method is compulsory to raise the electrocatalyst robustness and incorporate the M-N_x sites into a carbon backbone offering suitable electronic conductivity [30,33–35]. Moreover, high surface area and interconnected pores enabling mass transport of reactants toward the active sites represent essential prerequisites to achieve an appreciable electrocatalytic activity [36]. Although some nitrogen metal-free moieties can participate in the ORR mechanism (e.g. pyridinic units), it should be mentioned that overall the M-N_x constitute the most boosterish sites [12,35]. In this context, the choice of metal plays a pivotal role in the ORR mechanism. Previous studies on transition metal phthalocyanines (TMPc) place the FePc on top of the Volcano plot, thus suggesting that Fe-N_x-Cs could be the most active non-PGM catalysts among the TM-N-Cs [37]. Such a tremendous activity is related to the electronic structure of the metal center which promotes the rupture O=O bond as well as the empty d_{z^2} and filled d_{xy}, d_{yz} orbitals, which easily allow bonding with the π^*-electrons of the O_2 molecule [28]. From the selectivity point of view, it should be emphasized that FePc and MnPc promote the 4-electron ORR pathway due to their higher d-character while CoPc, NiPc, and CuPc enable the 2-electron fashion due to their ring character in the interacting frontal orbital [38].

Despite displaying high intrinsic activity per metal site, monometallic TM-N_x-C electrocatalysts own a low site density which limits the overall activity and applications [39]. In recent years, bimetallic-nitrogen carbon electrocatalysts (TM_1-TM_2-N_x-C) have been extensively studied due to their superior activity and stability compared to monometallic TM-N_x-Cs [40–54]. For instance, it has been proven that the addition of Co in Fe-N-C catalysts can hasten up the durability of the electrocatalysts in both acid and alkaline electrolytes [40,42]. However, the addition of Co slightly decreases the activity of Fe-N_x-C electrocatalysts and, as a major drawback, it increases the production of unwanted peroxide species [42,55]. Furthermore, Co is rated as a critical raw material (CRM) being fundamental for other applications, such as Li-ion batteries [56]. Unlike Co, the introduction of Mn in Fe-N-C electrocatalysts has beneficial effects on both the activity and selectivity. Kodali et al. prepared different TM1-TM2-N_x-Cs combining Co, Ni, Fe, and Mn and using 4-aminoantipyrine as a nitrogen-rich source to switch from the indirect 2 × 2-electron ORR transfer to the direct 4-electron transfer in microbial fuel cells (MFCs) [55]. The best metal combination resulted from Fe and Mn, which displayed the highest activity, the lowest H_2O_2 production in neutral electrolyte, and showed great durability performance in a real MFC. A similar result was found by Muhyuddin et al., who functionalized lignin-derived activated char with Mn (II) and Fe (II) phthalocyanines. The addition of Mn did not increase the kinetics of the Fe-N-C catalysts prepared with the same conditions but enhanced the limiting current and minimized the production of peroxide in both acid and alkaline environments [57]. In another study, it was shown that the improved catalytic activity of Mn-Fe-N_x-C compared to Fe-N_x-C electrocatalyst can result from a synergic dual cascade mechanism where the *OH intermediate adsorbed by Fe is transferred to adjacent Mn active site, thus overcoming the weak *OH adsorption on single Fe site [43].

In addition to the substitution of the PGM with earth-abundant metals, the development of low-cost carbon support from readily available biomass waste has sparked the interest of scientists [58–64]. Indeed, global food waste generation has become a relevant environmental issue in the last few decades accounting for 1.3 billion metric tons [65]. The uncontrolled generation of food waste could be alleviated by dealing with a circular economy paradigm aiming at upcycling waste into value-added products at minimum cost [66]. Among biomass waste, spent coffee grounds (SCGs) are solid residues obtained after brewing milled coffee beans [67]. SCG generation has reached up to 6 million tons and the major fraction ends up in landfills [68–70]. However, the direct disposal of a high amount of SCGs in landfills can cause serious environmental problems since some organic compounds, such as caffeine, tannins, and polyphenols are ecotoxic [69,71]. With its abundance of caffeine and proteins, SCGs represent a promising source of nitrogen that can benefit the ORR performance of PGM-free electrocatalysts [72]. As a matter of fact, N is an electron-rich atom that can interact with the nearby sp^2 carbon atoms via π - π interaction and donate electrons into graphene's matrix, thus tuning the electronic conductivity and catalytic activity [73,74]. By exploiting nitrogen-rich sources, such as waste coffee, *in situ* nitrogen doping is achievable, without the need for any further nitrogen precursor, like melamine, urea, *etc.* [74]. Apart from nitrogen doping, carbon produced by SCGs can be produced with a tailored micro/mesoporous ratio thus enabling efficient mass transport [75,76]. This requires a thorough control of the pyrolysis parameters, such as the target temperature. It has been recently reported that an enhancement in pyrolysis temperature leads to an increase in specific surface area (SSA) for different biomass sources, including coffee waste [63]. Specifically, for SCGs, it was found that the pyrolysis at 800 °C can result in 372 $m^2\ g^{-1}$ of SSA while exceeding that temperature a sintering effect diminishes porosity [76]. However, this SSA value is not high enough to permit a good exposition of the active sites, especially in the case of single-site catalysts. Therefore, SCG-based char needs to be activated by chemical agents, such as KOH, to achieve higher surface area and better ORR results [77].

Combining the benefits of a nitrogen-rich source like SCGs with the metallic synergy between Fe and Mn, in their atomically dispersed form, bimetallic SCG-derived electrocatalysts were herein designed by following a three-step synthesis: 1) pyrolysis of SCGs taken from *Illycaffè S.p.A.* at four different temperatures 400, 600, 800, 1000 °C, 2) activation of the as-obtained char with KOH to uplift the surface area and 3) functionalization of the activated carbon with 10 wt.% of Fe(II) phthalocyanine and 10 wt.% of Mn(II) phthalocyanine to create the ORR active sites within the carbon matrix. Even though SCGs have been already used to synthesize PGM-free materials for ORR [78,79], dual-site electrocatalysts with Fe and Mn prepared by mixing SCG-based carbon with Fe and Mn precursors have never been prepared. Moreover, the first pyrolysis temperature gives rise to carbon support possessing different morphological and chemical properties and therefore the electrochemical outcomes are expected to be different. Therefore, the effects of the first pyrolysis on the morphological properties and, most importantly, on the electrocatalytic performance in a cathodic semi-compartment via the rotating ring disk electrode (RRDE) technique was herein studied. Finally, the best-performing material was tested in a real membrane electrode assembly, as a proof of concept in the actual operation within AEMFC environment.

2. Experimental

2.1. Synthesis

SCGs were supplied by *illycaffè S.p.A.* company in Trieste, Italy. SCGs were sampled after espresso coffee brews prepared with 100 % *Coffea arabica* blend medium roasted by using a professional espresso coffee machine (Cimbali, Italy). SCGs were oven-dried at 103 °C up to complete dehydration. The SCG powder was poured into an alumina boat, which was put inside a quartz tube belonging to Naberthem®RSH 50/500/13 tubular furnace. N_2 gas was flushed for 30 min with a flow rate of 100 cm^3 min^{-1} to create an anoxic atmosphere. Afterward, the samples were pyrolyzed at the target temperature (400, 600, 800, 1000 °C) for 1 h by setting a rate of 5 °C min^{-1} and keeping the N_2 flux constant. The gravimetric yield of the process was calculated as the ratio between the output and input mass, and it varies upon the target temperature and the raw material. Thereafter, the obtained char was subject to chemical activation with a KOH/carbon weight ratio of 4:1. For this process, KOH was first dissolved in ethanol within a round bottom flask with two necks. After the dissolution of KOH, the char was added, and the mixture was stirred at room temperature for a period of time between 12 and 24 h. Subsequently, the temperature was raised to 80 °C upon stirring and a constant nitrogen flux to allow the evaporation of the solvent under a dry atmosphere. The dried mixture was chopped into small pieces and poured into an alumina boat covered with Ni strips to prevent probable reactions between aluminum oxide and the KOH embedded into the carbon at high temperatures. For a similar reason, the quartz tube where the activation was conducted was internally covered with a stainless-steel foil. After creating an inert atmosphere, as previously described, the temperature was brought to 700 °C with a ramp of 5 °C min^{-1} and dwelled for 1 h upon a nitrogen flux of 100 cm^3 min^{-1}. Thereupon, to completely remove KOH, the activated powder was acid washed in 1 M HCl and repeatedly rinsed with milli-Q water under vacuum filtration until pH 7 was reached. Subsequently, the washed sample was dried overnight in an oven. The functionalization step was performed by thoroughly mixing the activated char with 10 wt% of iron (II) phthalocyanine (FePc) and 10 wt% of manganese (II) phthalocyanine (MnPc). Afterward, the obtained mixture was treated at 600 °C for 1 h under the same conditions as the first pyrolysis.

2.2. Morphological characterization

To study the surface morphology of the final materials, a desktop scanning electron microscopy (SEM, Thermo Fisher Phenom G6, Eindhoven, Netherlands) equipped with a thermoionic CeB6 source was used. The images were acquired in secondary electron (SE) mode.

The crystallographic phases were investigated with X-ray diffraction (XRD, Rigaku Miniflex 600, Tokyo, Japan) owning a Cu source. The XRD patterns were acquired in the range of 10–80°.

Raman spectroscopy (Jobin Yvon, France) was carried out by employing a helium-neon laser source (632.8 nm of wavelength), a microscope (BX40, Olympus, Japan) equipped with an objective lens of 50x magnification (0.6 N.A.) to focus the laser on the sample, and a silicon CCD detector operating at a 200 K to collect the scattered signal (Sincerity, Jobin Yvon, France). The I_D/I_G ratio was calculated by dividing the absolute band intensity of D at 1330 cm^{-1} by that of G at 1600 cm^{-1}.

The qualitative inorganic elemental analysis was carried out with an X-rays fluorescence (XRF, Artax 200, Bruker, Billerica, MA, USA) possessing a Mo anode.

Elemental analysis was performed by using Elementar Vario Microcube Device.

The surface chemistry of the as synthesized electrocatalysts was analyzed by Physical Electronics (PHI) 5800–01 X-ray photoelectron spectrometer, employing Alk_α as a monochromatic X-ray source at a power of 350 W, as previously reported [80,81].

2.3. Electrochemical characterizations

2.3.1. Rotating ring disk electrode (RRDE) tests

The electrocatalytic performance was determined by exploiting the rotating ring disk electrode (RRDE) technique. This was performed in a Pine 250 mL glass cell assembled with an RRDE (Pine rotating electrode E6R2, USA), a saturated Ag/AgCl electrode and a graphite rod, functioning as working, reference and counter electrode, respectively. The electrodes were immersed in a 0.1 M KOH electrolyte and the experimental conditions were controlled by Pine WaveDriver 200 EIS Bipotentiostat/Galvanostat (USA) and Pine WaveVortex 10 rotator (USA). The RRDE used in this work was made of a concentric glassy carbon disk (0.2376 cm^2 geometric area) and a Pt ring (0.2356 cm^2 geometric area). Before using it, the RRDE was accurately polished with alumina paste on a cloth to achieve a flat flawless surface, followed by ultrasonication cleaning in milliQ water. The ink was prepared by suspending 5 mg of catalyst in a mixture of 985 μL isopropanol (Alfa Aesar, Ward Hill, MA, USA) and 15 μL of 5 wt% Nafion®D-520 (Alfa Aesar, USA), which was then sonicated with a probe sonicator for 10 min at 55 % pulse amplitude. Then, the RRDE was fabricated by drop-casting 28.5 μL of the ink containing the electrocatalyst with a final loading of 0.6 mg cm^{-2}. Before starting the measurements, the cell was bubbled with pure O_2 for 30 min. Subsequently, the electrocatalyst was activated by performing cyclic voltammetry at a scan rate of 100 mV s^{-1} upon a potential window ranging between +150 to −1050 mV vs. Ag/AgCl (potential ring hold at +150 mV vs. Ag/AgCl) until a stable signal was obtained. After electrocatalyst activation, linear sweep voltammetry (LSV) was recorded with a rotating speed of 1600 rpm at a scan rate of 5 mV s^{-1} within the same potential window. The measured potentials were thereafter reported vs reversible hydrogen electrode (RHE) using the following equation:

$$E(\text{vs. RHE}) = E(\text{vs. Ag / AgCl}) + 0.197 + 0.0591\ \text{pH}. \quad \text{(Eq. (1))}$$

In addition, the peroxide% and the number of transferred electrons were calculated according to the Eqs. (2) and 3 reported below:

$$Peroxide\% = \frac{200 \cdot \frac{I_{ring}}{N}}{I_{disk} + \frac{I_{ring}}{N}} \quad \text{(Eq. (2))}$$

$$n = \frac{4I_{disk}}{I_{disk} + \frac{I_{ring}}{N}} \quad \text{(Eq. (3))}$$

where I_{disk} is the disk current, I_{ring} is the ring current and N is the collection efficiency, which was 0.38 as reported by the supplier. To compare the electroactivity and selectivity with a PGM electrocatalyst, Pt/C (40 wt.% of Pt Alfa Aesar) 30 μg_{Pt} cm^{-2} was deposited on glassy carbon and the measurements were performed as described above.

The accelerated stability test (AST) was conducted with RRDE technique by setting 2000 cycles within the same potential window used for the linear sweep voltammetry at 1600 rpm and 50 mV s^{-1} in O_2 saturated electrolyte. The catalyst loading was kept constant at 0.6 mg cm^{-2}. For comparison, two LSVs were recorded before and after the 2000 cycles at 5 mV s^{-1}.

2.3.2. AEMFC tests

2.3.2.1. Electrodes and MEA preparation. The CFeMn_600 sample was used as a cathodic electrocatalyst, while a Pt/C (40 wt.% Alfa Aesar) as an anodic electrocatalyst. The catalytic inks were prepared by mixing in an ultrasonic bath the electrocatalysts with FAA3 ionomer by maintaining the electrocatalyst/ionomer ratio of 80/20 wt.%, as elsewhere reported [82,83]. The ink was deposited by a spray coating technique onto a Sigracet 25-BC gas diffusion layer (SGL). A CFeMn_600 loading of 4 mg cm^{-2}, and a Pt loading of 0.5 mg cm^{-2} were used for cathode and anode respectively. A Fumasep® FAA3–50 membrane (FuMa-Tech), previously exchanged for 1 h in 1 M KOH solution to obtain the

hydroxide form, was used as the electrolyte [84,85]. A cold press procedure was used to realize the membrane-electrode assemblies (MEAs) [86].

2.3.2.2. . MEA characterization. The prepared MEA was tested in a 5 cm^2 single cell, connected to a commercial test station (Fuel Cell Tech.) equipped with an electronic load. The AEMFC electrochemical tests in terms of polarisation and power density curves were performed at 60 °C, by feeding the cell with fully humidified H_2/O_2 with a flow rate of 1.5 and 2 times the stoichiometric value at each imposed current intensity.

3. Results and discussion

Fig. 1 reports the main steps of the bimetallic SCG-derived electrocatalysts, i.e. i) pyrolysis conducted at different temperatures, ii) KOH activation to create a 3D interconnected pore network and iii) functionalization with Fe(II)Pc and Mn(II)Pc to provide the electroactive sites. Regarding the first step, one of the most important features of biomass pyrolysis is the gravimetric yield obtained after the treatment, which was calculated as explained in Section 3.1. It should be noted that, even if this parameter refers only to the first stage of the electrocatalyst synthesis, yield is fundamental to figure out the scalability of the synthetic process at first glance and evaluate how much pristine waste material is transformed in solid biochar. The values reported in Table S1 show a descendent trend with temperature, as already observed in other works [76], but remain higher than 20 %, thus suggesting a possible scalability of the carbon material preparation from SCGs.

3.1. Morphological characterizations

Considering the final electrocatalysts, the morphological properties were thoroughly analyzed starting from the images acquired through scanning electron microscopy (SEM) (Fig. S1). All the samples are constituted of singular or aggregated particles displaying irregular shapes. The surface of these particles depicts an elevated degree of roughness and it is delimited by sharp and jagged edges.

The crystallographic structure of the as-synthesized electrocatalysts was analyzed via X-ray diffraction (XRD) and the results are depicted in Fig. 2a. All the spectra show one broad peak centered at ca. 23–24° arising from (002) graphitic carbon planes. In the case of CFeMn_400, a more visible broad hump at ca. 41–44° corresponding to (110) graphitic planes can be detected while for the other samples appear as a damp peak.

To gain insightful information on the carbonaceous structure of the electrocatalysts Raman spectroscopy was performed and the spectra are depicted in Fig. 2b. At first glance, every sample shows the appearance of two bands at ca.1326 cm^{-1} and 1576 cm^{-1}, called D and G bands, respectively. G band arises from the E_{2g} vibrational mode associated with the sp^2 C motions of the perfect graphitic lattice basal plane. The in-plane vibrations of carbon atoms near defects having A_{1g} symmetry set off the D band, as an indicator of a defective graphitic structure [87]. In the case of a high proportion of amorphous carbon, the two bands tend to overlap between 1400 and 1500 cm^{-1} leading to a valley V in the middle of the two bands, which indicates the occurrence of amorphous carbon [88]. As a conventional practice, the defectivity of carbon materials is determined with the I_D/I_G ratio. An I_D/I_G close to one indicates a high carbon structure defectivity. Interestingly, a linear correlation between the I_D/I_G ratio and the temperature of the first pyrolysis was found and reported in Fig. S2: the higher the temperature the higher the I_D/I_G indicating a higher level of graphitization. This result could indicate an enhancement in defectivity by increasing temperature [89].

To qualitatively assess the presence of the catalytic metallic centers, i.e. Fe and Mn, XRF spectra were acquired and reported in Fig. S3. The incorporation of Fe and Mn was ascertained by intense and sharp signals at 5.9, 6.4 KeV. The former is associated with the K_α transition in Mn atoms whereas the latter arises from the superimposition between K_β transition of Mn and the K_α transition of Fe atoms. No impurities were detected in CFeMn_400. On the contrary, some K traces were identified in the other samples as well as Ni and Cr impurities in CFeMn_1000. Potassium comes as the major impurity resulting from the KOH activation while Cr and Ni might derive from the furnace setup.

The quantification of the main elements in the final electrocatalysts, i.e. C, N, H and S, was performed by elemental analysis. The results displayed in Table S2 show the effect of the temperature on the composition. At 400 °C the amount of carbon is just above 71 % and it dramatically increases up to 80 % at 600 °C and its value almost stabilizes above this temperature. On the contrary, the amount of H decreases with temperature, especially between 400 and 600 °C. The content of nitrogen spans the interval 3.6–4.36 % and it does not show a precise trend. This element partially comes from the biomass source containing N-rich compounds and the addition of metal phthalocyanines.

The Fe and Mn content within functionalized samples was quantified by ICP-MS analysis and the results were reported in Table S3. The amount of the two metals shows dissimilarities among the samples being higher in CFeMn_800, where Mn and Fe are 3.94 and 2.75 wt%, respectively. CFeMn_600 shows slightly lower values, i.e. 3.29 and 2.52 wt% of Mn and Fe, while CFeMn_400 and CFeMn_1000 possess the least amount of metals, i.e. ≤ 1.

The surface of the nitrogen-enriched bimetallic samples derived from SCGs was analyzed by N1s and C1s high-resolution spectra. For N1s, the signals of 5 different nitrogen species were considered: imine at 397.5 ± 0.1 eV, pyridinic-N at 398.4 ± 0.1 eV, N_x–M (*M*=Fe, Mn) at 399.7 ± 0.1 eV, pyrrolic-N at 400.8 ± 0.1 eV, and graphitic-N at 402.3 ± 0.1 eV, as reported in the literature [80,81,90,91]. Fig. 3 and Table 1 show the deconvolution spectra and a summary of nitrogen speciation, respectively. The pyridinic/pyrrolic ratio is about 6.1 for CFeMn_400; whereas it is between 1.4 and 2.9 for the other catalysts. The most significative interaction between N-moieties and the metals (Fe, Mn) is encountered for CFeMn_800 with a relative percentage of 42.9 %, followed by CFeMn_400 and CFeMn_600. These interactions decrease for the catalyst treated at the highest temperature (CFeMn_1000).

As reported in the literature [91,92], the electrochemical activity in an alkaline environment of ORR is not strictly correlated to the chemistry of nitrogen. In contrast, the investigation of carbon speciation

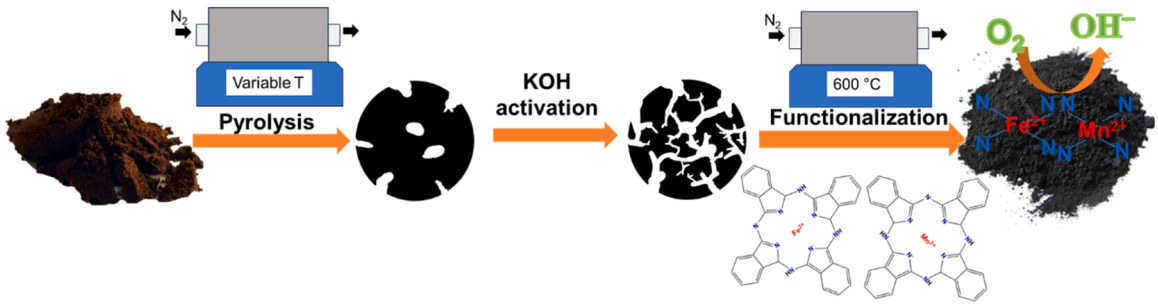

Fig. 1. Sketch of the main synthetic steps: pyrolysis of SCGs, KOH activation and functionalization with Mn(II)Pc and Fe(II)Pc.

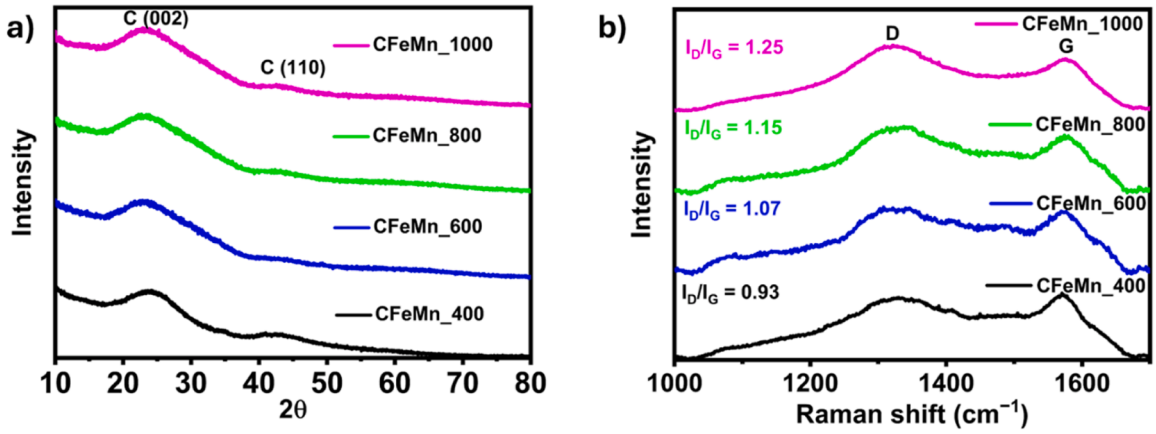

Fig. 2. (a) XRD patterns and (b) Raman spectra of the functionalized samples.

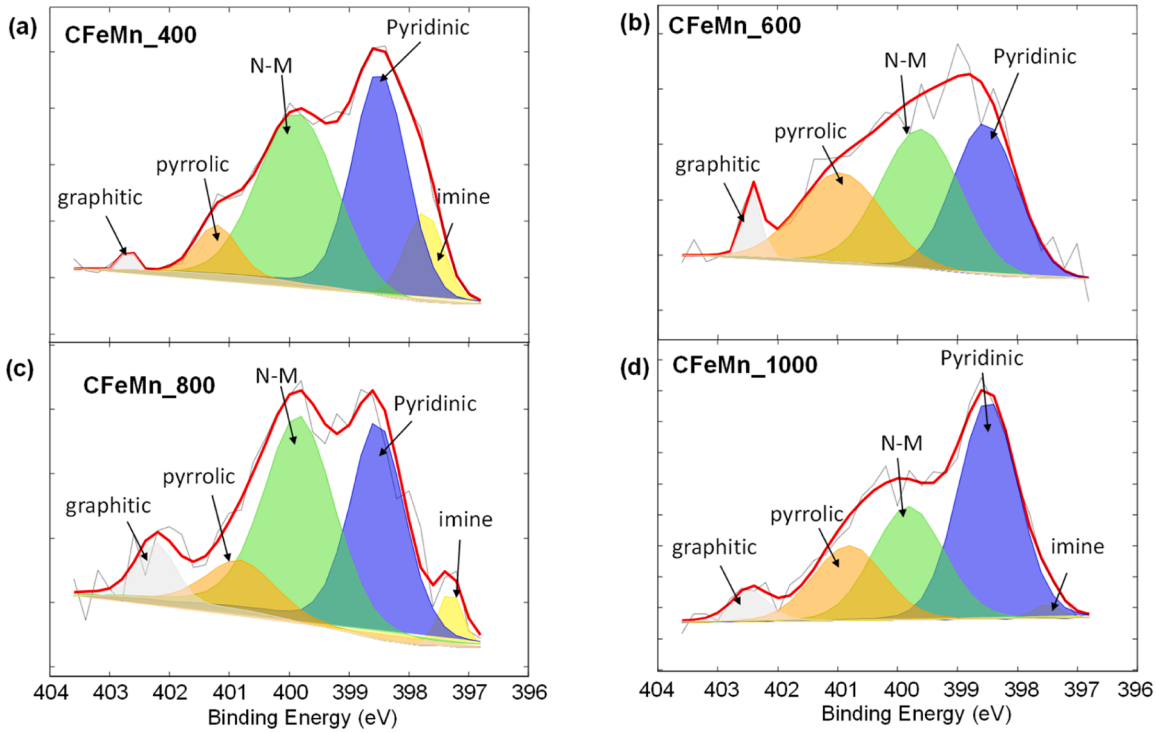

Fig. 3. Comparison of XPS N1s signals for the CFeMn electrocatalysts treated at (a) 400 °C, (b) 600 °C, (c) 800 °C and (d) 1000 °C.

Table 1
Nitrogen speciation from N1s deconvolution spectra.

Composition of N (relative%)						
Electrocatalysts	N (at.%)	Imine (397.5 eV)	Pyridinic (398.4 eV)	N-M (*M*=Fe, Mn) (399.7 eV)	Pyrrolic (400.8 eV)	Graphitic (402.3 eV)
CFeMn_400	5.6	10.8	40.0	41.7	6.5	1.1
CFeMn_600	2.8	–	34.5	36.1	25.4	4.0
CFeMn_800	3.4	4.5	34.3	42.9	11.8	6.5
CFeMn_1000	5.2	1.4	46.6	28.6	18.9	4.5

becomes the most important analysis for the correlation of performance to the surface characteristics. The considered binding energy, for C1s deconvolution reported in Fig. 4, corresponds to 284.3 eV for graphitic carbon, 285.0 eV for secondary carbons coordinated to carbon-nitrogen or carbon-oxides, 286.2 eV for CN_x defects, 287.1 eV for alcohol and ether groups (C-OH/C-OC), 288.1 eV for ketones or aldehydes (C=O) and 289.5 eV for carboxy species (COOH). CFeMn_1000 and CFeMn_400 have the largest content of graphitic carbon, whereas CFeMn_600 and CFeMn_800 have a significant content of C-N defects, more than double compared to the other two catalysts, as depicted in the histograms of Fig. S4. Among the different catalysts, there are no relevant changes in the composition of the oxidized species.

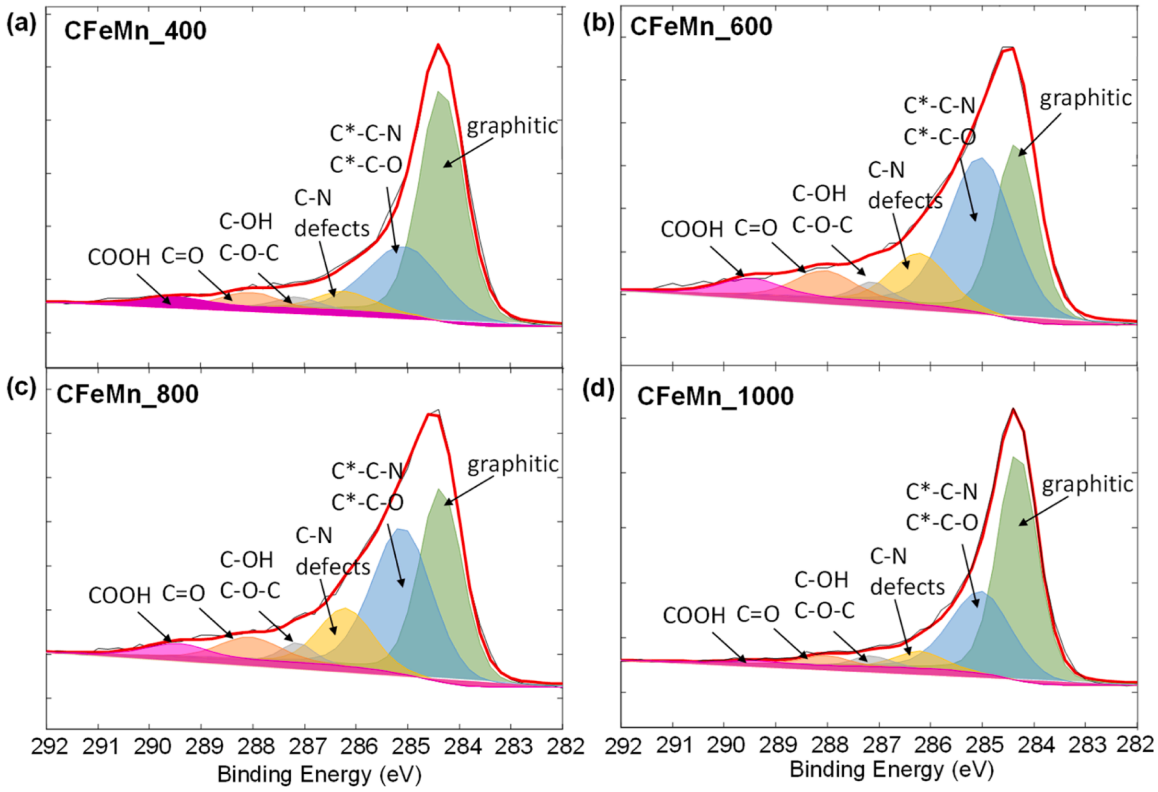

Fig. 4. Comparison of XPS C1s signals for the CFeMn catalysts treated at (a) 400 °C, (b) 600 °C, (c) 800 °C and (d) 1000 °C.

Fig. 5 shows the N_2 adsorption/desorption curves and the pore size distribution on the adsorbed volume of the electrocatalyst materials. Type I isotherms, displayed in Fig. 5a, are characteristics of microporous solids in which adsorption takes place even at low relative pressure for the strong interactions between the pore walls and the adsorbate. For all the catalysts, the pore filling occurs at a very low p/p° value (< 0.2) without capillary condensation. Furthermore, the low gaps between the absorption/desorption values suggest a hysteresis of type H4 where planar particles are agglomerated with a heterogeneous distribution. The Langmuir surface areas, normally employed as the reference for microporous structure, are very high for all the SCG-based bimetallic electrocatalysts. The values range from 968 to 1820 m^2/g. Fig. 5b shows the pore size distribution calculated by the Horvath-Kawazoe (HK) theory confirming the predominant microporous structure of the four investigated catalysts with pore size centered at around 0.5 nm and a few mesopores larger than 2.0 nm.

3.2. *Electrochemical results*

To clarify the responsiveness of the SCG-derived electrocatalysts towards ORR, RRDE tests were performed in 0.1 M KOH alkaline electrolyte by recording linear sweep voltammetry (LSV) curves of both disk and ring electrode under a rotation speed of 1600 rpm and a scan rate of 5 mV s^{-1}. Onset potential (E_{on}), and half-wave potential ($E_{1/2}$) are extrapolated by the LSV of disk current (J_{disk}) and used as key performance indicators. Herein, E_{on}, which is defined as the potential needed to trigger the ORR, was estimated at − 0.1 mA cm^{-2} while $E_{1/2}$ was determined by the maximum of the first derivative of J_{disk} curve, as

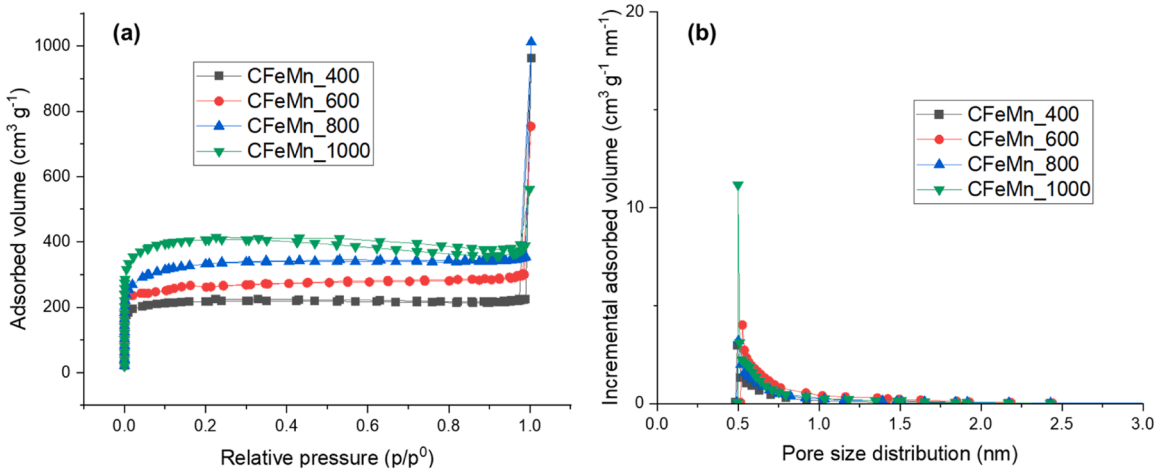

Fig. 5. (a) N_2 adsorption/desorption isotherms and (b) pore size distribution for CFeMn treated at different temperatures (400, 600, 800, and 1000 °C).

reported in other ORR protocols [93]. Additionally, the electrocatalyst can reach a current plateau called limiting current (J_{lim}). Upon the potential scan, peroxide can form according to the electrocatalyst selectivity and its generation can be assessed by using Eq. (2) (Section 2.3.1), which includes both the disk and the ring current (I_{ring}). Depending on the amount of peroxide produced, it is possible to discern whether ORR preferentially proceeds with a 2-electron or 4-electron pathway. As explained above, even the intermediate 2 × 2 mechanism can occur when O_2 is firstly reduced to HO_2^- and this one is further reduced to OH^-. This can be confirmed by monitoring the peroxide trend while scanning the potential.

3.2.1. Electrochemical results of the bimetallic SCG-derived electrocatalysts

The alkaline environment favors the ORR kinetics, compared to the acidic and neutral one, and sometimes the electrocatalytic activity of the PGM-free electrocatalysts can overcome that of Pt/C materials, rendering the AEMFCs more cost-effective. Hence, the electrocatalytic activity of the prepared electrocatalysts was compared with a Pt/C standard containing 40 wt.% of Pt. The J_{disk} and I_{ring} curves are illustrated in Fig. 6a and b, respectively, while the peroxide% and the number of transferred electrons (n) are displayed in Fig. 6c and d, respectively. At first glance, both CFeMn_600 and CFeMn_800 reach a J_{lim} of 4.1 and 3.4 mA cm^{-2} at 0.2 V vs RHE, respectively, thus displaying the typical LSV with a sigmoidal shape obtained upon rotation. On the contrary, CFeMn_400 and CFeMn_1000 do not reach a limiting current plateau within the set potential window, meaning that the electrochemical process is under the mixed kinetics-diffusion control even at low potentials. The kinetic parameters of the tested electrocatalysts, i.e. $E_{1/2}$ and E_{on}, are reported in Table 2. The values of $E_{1/2}$ follow this trend, i.e. CFeMn_600 ≈ CFeMn_800 > CFeMn_1000 > CFeMn_400, similarly to those of E_{on}, i.e. CFeMn_600 ≈ CFeMn_800 > CFeMn_400 > CFeMn_1000. Although CFeMn_600 and CFeMn_800 display the same $E_{1/2}$ and E_{on}, the CFeMn_600 develops higher currents at potentials < 0.8 V vs RHE, thus enlightening that CFeMn_600 is the most active electrocatalyst. Importantly, the $E_{1/2}$ of CFeMn_600 and CFeMn_800 is 0.866 V vs RHE, which is the same of Pt/C, whereas the E_{on} is 0.946 V vs RHE and thus lower than that of Pt/C (0.970 V vs RHE). This implies that the ORR kinetics of these PGM-free catalysts is comparable to that of Pt/C, thus spurring the replacement of Pt-based materials in AEMFCs. While CFeMn_600 and CFeMn_800 achieve similar results to Pt/C, the remaining electrocatalysts, i.e. CFeMn_400 and CFeMn_1000, depict lower currents upon the entire potential scan, thus highlighting a worse performance. The lowest activity of CFeMn_1000 could be attributed to the much lower relative content of M-N_x units present in the electrocatalysts, i.e. 28.1 % vs > 35 % for the other electrocatalysts (Table 4). As a matter of fact Nx-M units represent the most active sites of ORR and therefore a lack of these units can easily lead to poor catalytic performance [12]. On the other hand, the low currents achieved by CFeMn_400 could be due to the lower surface area,

Table 2
Electrochemical data of the functionalized samples compared with Pt/C standard: [a] E_{on} stands for onset potential; [b] $E_{1/2}$ stands for half-wave potential.

Sample	$E_{on}^{[a]}$ [V vs RHE]	$E_{1/2}^{[b]}$ [V vs RHE]
Pt/C	0.970	0.866
CFeMn_400	0.945	0.786
CFeMn_600	0.946	0.866
CFeMn_800	0.946	0.866
CFeMn_1000	0.926	0.766

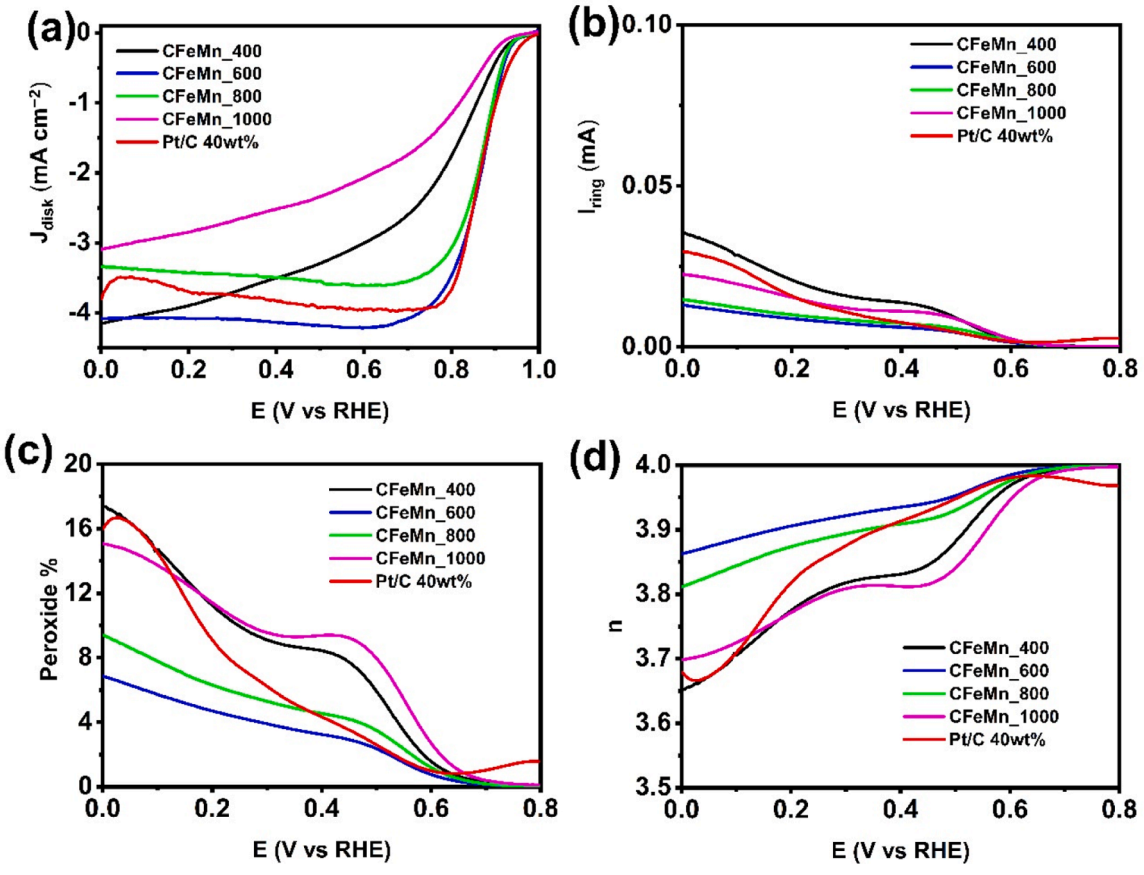

Fig. 6. RRDE results of the functionalized samples in 0.1 M KOH: (a) Disk current density and (b) Ring current recorded at 1600 rpm and 5 mV s^{-1}; (c) Peroxide% and (d) number of transferred electrons (n).

which is less than 1000 $m^2 g^{-1}$ and higher for the other electrocatalysts [94].

From the selectivity point of view, the peroxide% stays lower than 20 % and n does not go below 3.50. The peroxide% trend, the single-step shaped J_{disk} curve and the absence of the I_{ring} peak at 0.9 V vs RHE point out that a direct 4-electron transfer occurs on the surface of the synthesized electrocatalysts (especially CFeMn_600 and CFeMn_800), bypassing the formation of HO_2^- intermediate [95–97]. The minimized peroxide production (below 5 %) and the maximized n (> 3.85) make CFeMn_600 the most selective electrocatalyst, thus suggesting CFeMn_600 as the most eligible candidate for AEMFCs cathode. To the best of our knowledge, the highest activity and selectivity of CFeMn_600 and CFeMn_800 toward the 4-electron pathway could be due to the higher content of C-N defects compared to CFeMn_400 and CFeMn_1000, which showed a higher content of graphitic carbon, as depicted in Fig. S4. Although the electroactivity is mostly related to the amount of M-N_x moieties, the intrinsic defects in sp^2 carbon, created by electron-rich nitrogen atoms, can activate the carbon π electrons by conjugating with the lone-pair electrons from N dopants [98]. Therefore, the C atoms adjacent to N atoms become more active for ORR than the C atoms, thus explaining why electrocatalysts with more C-N defects result to be more performing than the ones with higher graphitic content. Another reason explaining the highest activity of CFeMn_600 and CFeMn_800 over CFeMn_400 and CFeMn_1000 might be the higher amount of metals (i.e. Mn and Fe), which is at least 2 wt% units higher in CFeMn_600 and CFeMn_800 than CFeMn_400 and CFeMn_1000.

3.2.2. *Electrochemical results of the only pyrolyzed and activated SCG-derived carbons*

For the sake of comparison, the results of the only pyrolyzed and activated SCG-based carbons are reported in Supplementary material (Table S4 and Figs. S5, S6). The catalytic performance of the pyrolyzed and activated samples is not comparable with that of the functionalized bimetallic electrocatalyst as it can be deduced by the values reported in Table S4. The activity in terms of $E_{1/2}$ and E_{on} improves after the activation due to the enhancement of porosity, which favors the pore accessibility to oxygen molecules. The functionalization of carbon with Fe and Mn phthalocyanine boosts the activity performance of the carbon electrocatalyst and minimizes the production of peroxide species due to the introduction of Fe-N_x and Mn-N_x electroactive centers. Comparing the activated carbons, it can be observed that $E_{1/2}$ and E_{on} range between 0.776 – 0.791 V vs RHE and 0.831 – 0.851 V vs RHE respectively (Table S4). Considering the values in Table S4, the electrocatalytic activity follows this trend: CA_600 ≈ CA_800 > CA_400 > CA_1000. The peroxide% production (Fig. S5c) shows a maximum between 0.6 – 0.7 V vs RHE and then it decreases monotonically at lower potentials reaching up to 30 % ca. at 0 V vs RHE for all catalysts apart from CA_600 where it plummets to 15 % at the same potential. The opposite trend was observed for the number of transferred electrons where the electrocatalysts reached the minimum value of 2.75 ca. (Fig. S5d). From these results and the two-step J_{disk} curves (Fig. S5a), it can be inferred that the mechanism is mainly 2 × 2-electron, meaning that oxygen is reduced to HO_2^- at higher potentials and then to H_2O at lower potentials. The comparison of the only pyrolyzed samples shows the following trend in the electrocatalytic activity: C_1000 > C_800 > C_600 > C_400, as it can be deduced by the $E_{1/2}$ and E_{on} numbers of Table S4, ranging between 0.631 and 0.771 V vs RHE and 0.581 – 0.671 V vs RHE respectively. These values are by far lower than those recorded for the activated and functionalized samples. In addition, the limiting current densities of J_{disk} are < 1.5 mA cm^{-2} (Fig. S6a) and therefore extremely lower compared to those of the functionalized samples, proving that the only pyrolyzed samples are poorly electroactive materials. Moreover, the only pyrolyzed samples are not suitable for fuel cell application since the amount of peroxide is too high. Indeed, peroxide% remains at values higher than 50 % throughout the potential window for all catalysts (Fig. S6c) and n stay below 3 (Fig. S6d), thus confirming a predominant 2-electron transfer.

To validate the importance of KOH activation in the electroactivity of the electrocatalyst, C_600 was directly blended with 10 wt% of FePc and 10 wt% of MnPc and the mixture was heat treated at 600 °C for 1 h. The resulting material was labeled as CFeMn_noA_600 and its performance was compared with CFeMn_600 in Fig. S7, reported in the Supporting Information. From the LSV curve (Fig. S7a), the peroxide production (Fig. S7c) and transferred electrons (Fig. S7d), CFeMn_noA_600 shows very low performance compared to CFeMn_600. Indeed, the current developed by CFeMn_noA_600 is much lower than CFeMn _600 and the peroxide production of CFeMn_noA_600 is twice as CFeMn _600, meaning that CFeMn_noA_600 exhibits much lower activity and selectivity for 4-electron route than CFeMn _600. This outcome could be related to the lower surface area of the non-activated carbon and therefore confirms the importance of performing KOH activation to achieve high electroactivity of the material.

3.2.3. *Stability test*

Along with activity and selectivity, durability is a fundamental requirement for its implementation in fuel cell devices. Therefore, an accelerated stability test of 2000 cycles at 50 mV s^{-1} in the potential range 1.0 V to 0 V vs RHE was performed on the topmost material, i.e. CFeMn_600, and the results are illustrated in Fig. S8. Although some changes were detected in the J_{disk} limiting current (Fig. S8a), in the peroxide% (Fig. S8c) and in the number of transferred electrons (Fig. S8d), the electrocatalytic activity is retained after 2000 cycles as the $E_{1/2}$ and E_{on} show a slight shift of ca. 5 mV towards less positive values. This finding confirms the kinetic robustness of this electrocatalyst upon cycling even though the stability of the mass transfer zone should be improved.

3.2.4. *Fuel cell test*

Fig. 7 shows the I–V and power density curves obtained when the sample CFeMn-600 was assembled at the cathode side of the AEMFC. The test was carried out by feeding the cell with H_2 and O_2 at 60 °C and 100 % of relative humidity (RH). The open circuit voltage (OCV) value of 0.890 V is slightly lower than that normally obtained under these conditions when Pt (1.00 V) or non-PGM carbon-based materials (0.920 V) were used as a cathodic electrocatalyst. A maximum power density of 30 mWcm^{-2} was reached. Comparing the performance with other synthesized TM-N-C catalysts, reported in literature [82,99–105], assembled with FUMASEP® FAA-3–50 membrane, the CFeMn_600 sample shows lower power density values. It is worth noting that this material derives from a natural source such as SCGs and not from lab synthesis, making it a promising innovative biomaterial. A comparison between CFeMn_600 and a few biomass-based PGM-free electrocatalysts tested in similar conditions was reported in Table S5. Our best-performing material showed similar or even better results compared to some tested

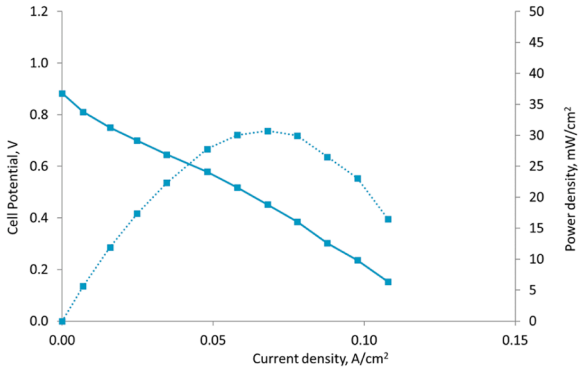

Fig. 7. I-V and power density curves for CFeMn-600 catalysts at 60 °C for an AEMFC fed with H_2 and O_2 (1.0 bar abs, 100 % RH).

electrocatalysts but did not reach the highest achieved performance in terms of maximum power density. It should be noted that SCG-based electrocatalysts have never been tested in AEMFCs. Therefore, further studies should be done to optimize the material properties of SCG-carbon materials, such as the electronic conductivity of the carbonaceous platform.

4. Conclusion

Four bimetallic electrocatalysts were prepared by pyrolyzing spent coffee grounds, as a carbon and nitrogen source, at 400, 600, 800, and 1000 °C. The subsequent activation with KOH and functionalization with the simultaneous addition of FePc and MnPc lead to microporous, amorphous and carbon-defective structures. An outstanding performance was achieved in half-cell compartment by CFeMn_600 which displayed an $E_{1/2}$ of 0.866 V vs RHE and J_{lim} comparable to that of Pt/C containing a 40 wt.% of Pt. From the selectivity point of view, CFeMn_600 showed the lowest production of peroxide (< 5 %) and the highest number of transferred electrons (3.9), thus making this electrocatalyst more selective compared to the Pt counterpart. These splendid outcomes resulted from a trade-off between its morphology and surface chemistry. Indeed, it possesses a surface area larger than 1000 $m^2 g^{-1}$, and from the chemistry point of view the synergistic action of Fe and Mn and the occurrence of C-N defects inside the carbon structure contributed to an excellent RRDE performance. From the durability point of view, the electrocatalyst showed a limiting current shift but it retained $E_{1/2}$ and E_{on}. This is an appreciable result, but more work should be done in order to prevent any current shift in the mass transport region. Despite the successful results in half-cell compartment, the OCV and the peak of power density reached in AEFMC are not comparable with the best state-of-art PGM-free electrocatalysts. In any case, the analysis of fuel cell performance has never been reported for PGM-free electrocatalysts derived from SCG waste and these results can be considered as a pretext to ameliorate the performance of electrocatalysts to match the market needs.

CRediT authorship contribution statement

Giovanni Zuccante: Writing – review & editing, Writing – original draft, Formal analysis, Data curation, Conceptualization. **Maurizio Acciarri:** Formal analysis, Data curation, Conceptualization. **Carmelo Lo Vecchio:** Writing – review & editing, Writing – original draft, Investigation, Formal analysis, Data curation. **Irene Gatto:** Writing – review & editing, Writing – original draft, Investigation, Formal analysis, Data curation. **Vincenzo Baglio:** Writing – review & editing, Writing – original draft, Investigation, Formal analysis, Data curation. **Nicolò Pianta:** Writing – review & editing, Writing – original draft, Investigation, Formal analysis, Data curation. **Riccardo Ruffo:** Writing – review & editing, Writing – original draft, Methodology, Formal analysis, Data curation. **Luciano Navarini:** Writing – original draft, Resources, Methodology, Investigation, Formal analysis, Conceptualization. **Carlo Santoro:** Writing – review & editing, Writing – original draft, Supervision, Resources, Project administration, Methodology, Funding acquisition, Conceptualization.

Declaration of competing interest

The authors declare that they have no known competing financial interests or personal relationships that could have appeared to influence the work reported in this paper.

Data availability

Data will be made available on request.

Acknowledgments

G.Z. acknowledges a Ph.D. scholarship on the Italian National Ph.D. program “Scientific, technological and social methods enabling circular economy”, Curriculum “Technical materials for circularity” funded by Italy’s Recovery and Resilient Plan and EU Recovery Plan. C.S. would like to thank the support from ENEA – UNIMIB agreement (Procedure 1.1.3 PNRR POR H2). C.S. would like to also acknowledge the Cariplo Foundation, Call for Circular Economy through the project “Transformation of plastic waste in Electrocatalysts, Supported by exhausted gases recovery Layout” (TESLA).

Supplementary materials

Supplementary material associated with this article can be found, in the online version, at doi:10.1016/j.electacta.2024.144353.

References

[1] A.G. Olabi, T. Wilberforce, M.A. Abdelkareem, Fuel cell application in the automotive industry and future perspective, Energy 214 (2021) 118955, https://doi.org/10.1016/j.energy.2020.118955.
[2] J.M. Andújar, F. Segura, Fuel cells: history and updating. A walk along two centuries, Renew. Sustain. Energy Rev. 13 (2009) 2309–2322, https://doi.org/10.1016/j.rser.2009.03.015.
[3] C. Santoro, A. Lavacchi, P. Mustarelli, V. Di Noto, L. Elbaz, D.R. Dekel, F. Jaouen, What is next in anion-exchange membrane water electrolyzers? Bottlenecks, benefits, and future, ChemSusChem 15 (2022), https://doi.org/10.1002/cssc.202200027.
[4] A. Sarapuu, J. Lilloja, S. Akula, J.H. Zagal, S. Specchia, K. Tammeveski, Recent advances in non-precious metal single-atom electrocatalysts for oxygen reduction reaction in low-temperature polymer-electrolyte fuel cells, ChemCatChem 15 (2023), https://doi.org/10.1002/cctc.202300849.
[5] A. Sarapuu, E. Kibena-Põldsepp, M. Borghei, K. Tammeveski, Electrocatalysis of oxygen reduction on heteroatom-doped nanocarbons and transition metal-nitrogen-carbon catalysts for alkaline membrane fuel cells, J. Mater. Chem. A Mater. 6 (2018) 776–804, https://doi.org/10.1039/c7ta08690c.
[6] M.M. Hossen, M.S. Hasan, M.R.I. Sardar, J. bin Haider, K.Tammeveski Mottakin, P. Atanassov, State-of-the-art and developmental trends in platinum group metal-free cathode catalyst for anion exchange membrane fuel cell (AEMFC), Appl. Catal. B 325 (2023), https://doi.org/10.1016/j.apcatb.2022.121733.
[7] A.T. Hamada, M.F. Orhan, A.M. Kannan, Alkaline fuel cells: status and prospects, Energy Rep. 9 (2023) 6396–6418, https://doi.org/10.1016/j.egyr.2023.05.276.
[8] T.B. Ferriday, P.H. Middleton, Alkaline fuel cell technology - A review, Int. J. Hydrog. Energy 46 (2021) 18489–18510, https://doi.org/10.1016/j.ijhydene.2021.02.203.
[9] H.A. Firouzjaie, W.E. Mustain, Catalytic advantages, challenges, and priorities in alkaline membrane fuel cells, ACS Catal. 10 (2020) 225–234, https://doi.org/10.1021/acscatal.9b03892.
[10] X. Ge, A. Sumboja, D. Wuu, T. An, B. Li, F.W.T. Goh, T.S.A. Hor, Y. Zong, Z. Liu, Oxygen reduction in alkaline media: from mechanisms to recent advances of catalysts, ACS Catal. 5 (2015) 4643–4667, https://doi.org/10.1021/acscatal.5b00524.
[11] Y. Li, Q. Li, H. Wang, L. Zhang, D.P. Wilkinson, J. Zhang, Recent progresses in oxygen reduction reaction electrocatalysts for electrochemical energy applications, Electrochem. Energy Rev. 2 (2019) 518–538, https://doi.org/10.1007/s41918-019-00052-4.
[12] T. Asset, P. Atanassov, Iron-nitrogen-carbon catalysts for proton exchange membrane fuel cells, Joule 4 (2020) 33–44, https://doi.org/10.1016/j.joule.2019.12.002.
[13] G. Daniel, T. Kosmala, M.C. Dalconi, L. Nodari, D. Badocco, P. Pastore, A. Lorenzetti, G. Granozzi, C. Durante, Upcycling of polyurethane into iron-nitrogen-carbon electrocatalysts active for oxygen reduction reaction, Electrochim. Acta 362 (2020) 137200, https://doi.org/10.1016/j.electacta.2020.137200.
[14] J. Masa, A. Zhao, X. Wei, M. Muhler, W. Schuhmann, Metal-free catalysts for oxygen reduction in alkaline electrolytes: influence of the presence of Co, Fe, Mn and Ni inclusions, Electrochim. Acta 128 (2014) 271–278, https://doi.org/10.1016/j.electacta.2013.11.026.
[15] V.P. Vasiliev, R.A. Manzhos, V.K. Kochergin, A.G. Krivenko, E.N. Kabachkov, A. V. Kulikov, Y.M. Shulga, G.L. Gutsev, A facile synthesis of noble-metal-free catalyst based on nitrogen doped graphene oxide for oxygen reduction reaction, Materials 15 (2022), https://doi.org/10.3390/ma15030821.
[16] S. Rojas-Carbonell, C. Santoro, A. Serov, P. Atanassov, Transition metal-nitrogen-carbon catalysts for oxygen reduction reaction in neutral electrolyte, Electrochem. Commun. 75 (2017) 38–42, https://doi.org/10.1016/j.elecom.2016.12.011.
[17] Y. Zhang, J. Parrondo, S. Sankarasubramanian, V. Ramani, Detection of reactive oxygen species in anion exchange membrane fuel cells using *in situ* fluorescence

spectroscopy, ChemSusChem 10 (2017) 3056–3062, https://doi.org/10.1002/cssc.201700760.
[18] C. Li, H. Tan, J. Lin, X. Luo, S. Wang, J. You, Y.M. Kang, Y. Bando, Y. Yamauchi, J. Kim, Emerging Pt-based electrocatalysts with highly open nanoarchitectures for boosting oxygen reduction reaction, Nano Today 21 (2018) 91–105, https://doi.org/10.1016/j.nantod.2018.06.005.
[19] G.N. Vayssilov, Y. Lykhach, A. Migani, T. Staudt, G.P. Petrova, N. Tsud, T. Skála, A. Bruix, F. Illas, K.C. Prince, V. Matolín, K.M. Neyman, J. Libuda, Support nanostructure boosts oxygen transfer to catalytically active platinum nanoparticles, Nat. Mater. 10 (2011) 310–315, https://doi.org/10.1038/nmat2976.
[20] A. Sajid, E. Pervaiz, H. Ali, T. Noor, M.M. Baig, A perspective on development of fuel cell materials: electrodes and electrolyte, Int. J. Energy Res. 46 (2022) 6953–6988, https://doi.org/10.1002/er.7635.
[21] U. Martinez, S. Komini Babu, E.F. Holby, H.T. Chung, X. Yin, P. Zelenay, Progress in the development of Fe-based PGM-free electrocatalysts for the oxygen reduction reaction, Adv. Mater. 31 (2019), https://doi.org/10.1002/adma.201806545.
[22] L. Yang, J. Shui, L. Du, Y. Shao, J. Liu, L. Dai, Z. Hu, Carbon-based metal-free ORR electrocatalysts for fuel cells: past, present, and future, Adv. Mater. 31 (2019), https://doi.org/10.1002/adma.201804799.
[23] D. Liu, L. Tao, D. Yan, Y. Zou, S. Wang, Recent advances on non-precious metal porous carbon-based electrocatalysts for oxygen reduction reaction, ChemElectroChem 5 (2018) 1775–1785, https://doi.org/10.1002/celc.201800086.
[24] M. Muhyuddin, D. Testa, R. Lorenzi, G.M. Vanacore, F. Poli, F. Soavi, S. Specchia, W. Giurlani, M. Innocenti, L. Rosi, C. Santoro, Iron-based electrocatalysts derived from scrap tires for oxygen reduction reaction: evolution of synthesis-structure-performance relationship in acidic, neutral and alkaline media, Electrochim. Acta 433 (2022) 141254, https://doi.org/10.1016/j.electacta.2022.141254.
[25] M. Muhyuddin, P. Mustarelli, C. Santoro, Recent advances in waste plastic transformation into valuable platinum-group metal-free electrocatalysts for oxygen reduction reaction, ChemSusChem 14 (2021) 3785–3800, https://doi.org/10.1002/cssc.202101252.
[26] S. Rojas-Carbonell, K. Artyushkova, A. Serov, C. Santoro, I. Matanovic, P. Atanassov, Effect of pH on the activity of platinum group metal-free catalysts in oxygen reduction reaction, ACS Catal. 8 (2018) 3041–3053, https://doi.org/10.1021/acscatal.7b03991.
[27] E. Berretti, M. Longhi, P. Atanassov, D. Sebastián, C. Lo Vecchio, V. Baglio, A. Serov, A. Marchionni, F. Vizza, C. Santoro, A. Lavacchi, Platinum group metal-free Fe-based (Fe[sbnd]N[sbnd]C) oxygen reduction electrocatalysts for direct alcohol fuel cells, Curr. Opin. Electrochem. 29 (2021), https://doi.org/10.1016/j.coelec.2021.100756.
[28] H.Y. Wang, C.C. Weng, Z.Y. Yuan, Insights into efficient transition metal-nitrogen/carbon oxygen reduction electrocatalysts, J. Energy Chem. 56 (2021) 470–485, https://doi.org/10.1016/j.jechem.2020.08.030.
[29] M. Mazzucato, G. Daniel, A. Mehmood, T. Kosmala, G. Granozzi, A. Kucernak, C. Durante, Effects of the induced micro- and meso-porosity on the single site density and turn over frequency of Fe-N-C carbon electrodes for the oxygen reduction reaction, Appl. Catal. B 291 (2021), https://doi.org/10.1016/j.apcatb.2021.120068.
[30] M. Muhyuddin, J. Filippi, L. Zoia, S. Bonizzoni, R. Lorenzi, E. Berretti, L. Capozzoli, M. Bellini, C. Ferrara, A. Lavacchi, C. Santoro, Waste Face surgical mask transformation into crude oil and nanostructured electrocatalysts for fuel cells and electrolyzers, ChemSusChem 15 (2022), https://doi.org/10.1002/cssc.202102351.
[31] M.M. Hossen, K. Artyushkova, P. Atanassov, A. Serov, Synthesis and characterization of high performing Fe-N-C catalyst for oxygen reduction reaction (ORR) in alkaline exchange membrane fuel cells, J. Power Sources 375 (2018) 214–221, https://doi.org/10.1016/j.jpowsour.2017.08.036.
[32] L. Peles-Strahl, Y. Persky, L. Elbaz, Design of advanced aerogel structures for oxygen reduction reaction electrocatalysis, SusMat 3 (2023) 44–57, https://doi.org/10.1002/sus2.104.
[33] W. Orellana, C.Z. Loyola, J.F. Marco, F. Tasca, Evidence of carbon-supported porphyrins pyrolyzed for the oxygen reduction reaction keeping integrity, Sci. Rep. 12 (2022), https://doi.org/10.1038/s41598-022-11820-6.
[34] S. Zago, M. Bartoli, M. Muhyuddin, G.M. Vanacore, P. Jagdale, A. Tagliaferro, C. Santoro, S. Specchia, Engineered biochar derived from pyrolyzed waste tea as a carbon support for Fe-N-C electrocatalysts for the oxygen reduction reaction, Electrochim. Acta 412 (2022) 140128, https://doi.org/10.1016/j.electacta.2022.140128.
[35] M. Muhyuddin, E. Berretti, S.A. Mirshokraee, J. Orsilli, R. Lorenzi, L. Capozzoli, F. D'Acapito, E. Murphy, S. Guo, P. Atanassov, A. Lavacchi, C. Santoro, Formation of the active site structures during pyrolysis transformation of Fe-phthalocyanine into Fe-Nx-C electrocatalysts for the oxygen reduction reaction, Appl. Catal. B 343 (2024), https://doi.org/10.1016/j.apcatb.2023.123515.
[36] G. Daniel, E. Foltran, R. Brandiele, L. Nodari, R. Pilot, E. Menna, G.A. Rizzi, A. Ahmed Isse, C. Durante, A. Gennaro, Platinum-free electrocatalysts for oxygen reduction reaction: fe-Nx modified mesoporous carbon prepared from biosources, J. Power Sources 402 (2018) 434–446, https://doi.org/10.1016/j.jpowsour.2018.09.060.
[37] L. Yang, D. Cheng, H. Xu, X. Zeng, X. Wan, J. Shui, Z. Xiang, D. Cao, Unveiling the high-activity origin of single-atom iron catalysts for oxygen reduction reaction, Proc. Natl. Acad. Sci. U S. A. 115 (2018) 6626–6631, https://doi.org/10.1073/pnas.1800771115.
[38] K. Singh, F. Razmjooei, J.S. Yu, Active sites and factors influencing them for efficient oxygen reduction reaction in metal-N coordinated pyrolyzed and non-pyrolyzed catalysts: a review, J. Mater. Chem. A Mater. 5 (2017) 20095–20119, https://doi.org/10.1039/c7ta05222g.
[39] H. Xu, D. Wang, P. Yang, A. Liu, R. Li, Y. Li, L. Xiao, X. Ren, J. Zhang, M. An, Atomically dispersed M-N-C catalysts for the oxygen reduction reaction, J. Mater. Chem. A Mater. 8 (2020) 23187–23201, https://doi.org/10.1039/d0ta08732g.
[40] S. Yang, X. Xue, J. Zhang, X. Liu, C. Dai, Q. Xu, J. Lian, Y. Zhao, G. Li, H. Li, S. Yuan, Molten salt "boiling" synthesis of surface decorated bimetallic-nitrogen doped carbon hollow nanospheres: an oxygen reduction catalyst with dense active sites and high stability, Chem. Eng. J. 395 (2020), https://doi.org/10.1016/j.cej.2020.125064.
[41] K. Zhao, Y. Shu, F. Li, G. Peng, Bimetallic catalysts as electrocatalytic cathode materials for the oxygen reduction reaction in microbial fuel cell: a review, Green Energy Environ. (2022), https://doi.org/10.1016/j.gee.2022.10.007.
[42] M. Gollasch, J. Müller-Hülstede, H. Schmies, D. Schonvogel, P. Wagner, A. Dyck, M. Wark, Elucidating synergistic effects of different metal ratios in bimetallic fe/co-n-c catalysts for oxygen reduction reaction, Catalysts 11 (2021), https://doi.org/10.3390/catal11070841.
[43] Z. Chen, X. Liao, C. Sun, K. Zhao, D. Ye, J. Li, G. Wu, J. Fang, H. Zhao, J. Zhang, Enhanced performance of atomically dispersed dual-site Fe-Mn electrocatalysts through cascade reaction mechanism, Appl. Catal. B 288 (2021), https://doi.org/10.1016/j.apcatb.2021.120021.
[44] X. Yang, C. Priest, Y. Hou, G. Wu, Atomically dispersed dual-metal-site PGM-free electrocatalysts for oxygen reduction reaction: opportunities and challenges, SusMat 2 (2022) 569–590, https://doi.org/10.1002/sus2.69.
[45] S.A. Mirshokraee, M. Muhyuddin, R. Lorenzi, G. Tseberlidis, C. Lo Vecchio, V. Baglio, E. Berretti, A. Lavacchi, C. Santoro, Litchi-derived platinum group metal-free electrocatalysts for oxygen reduction reaction and hydrogen evolution reaction in alkaline media, SusMat 3 (2023) 248–262, https://doi.org/10.1002/sus2.121.
[46] J. Lilloja, E. Kibena-Põldsepp, A. Sarapuu, A. Konovalova, M. Käärik, J. Kozlova, P. Paiste, A. Kikas, A. Treshchalov, J. Aruväli, A. Zitolo, J. Leis, A. Tamm, V. Kisand, S. Holdcroft, K. Tammeveski, Transition-metal and nitrogen-doped carbon nanotube/graphene composites as cathode catalysts for anion-exchange membrane fuel cells, ACS Appl. Energy Mater. 6 (2023) 5519–5529, https://doi.org/10.1021/acsaem.3c00613.
[47] K. Muuli, A. Sokka, M. Mooste, J. Lilloja, V. Gudkova, M. Käärik, M. Otsus, A. Kikas, V. Kisand, A. Tamm, J. Leis, A. Krumme, S. Holdcroft, J.H. Zagal, K. Tammeveski, Iron and cobalt phthalocyanine embedded electrospun carbon nanofiber-based catalysts for anion exchange membrane fuel cell cathode, J. Catal. 422 (2023) 117–130, https://doi.org/10.1016/j.jcat.2023.04.008.
[48] R. Kumar, M. Mooste, Z. Ahmed, S. Akula, I. Zekker, M. Marandi, M. Käärik, J. Leis, A. Kikas, A. Treshchalov, M. Otsus, J. Aruväli, V. Kisand, A. Tamm, K. Tammeveski, Highly active ZIF-8@CNT composite catalysts as cathode materials for anion exchange membrane fuel cells, Ind. Chem. Mater. 1 (2023) 526–541, https://doi.org/10.1039/d3im00081h.
[49] A. Sokka, M. Mooste, M. Käärik, V. Gudkova, J. Kozlova, A. Kikas, V. Kisand, A. Treshchalov, A. Tamm, P. Paiste, J. Aruväli, J. Leis, A. Krumme, S. Holdcroft, S. Cavaliere, F. Jaouen, K. Tammeveski, Iron and cobalt containing electrospun carbon nanofibre-based cathode catalysts for anion exchange membrane fuel cell, Int. J. Hydrog. Energy 46 (2021) 31275–31287, https://doi.org/10.1016/j.ijhydene.2021.07.025.
[50] J. Lilloja, M. Mooste, E. Kibena-Põldsepp, A. Sarapuu, A. Kikas, V. Kisand, M. Käärik, J. Kozlova, A. Treshchalov, P. Paiste, J. Aruväli, J. Leis, A. Tamm, S. Holdcroft, K. Tammeveski, Cobalt-, iron- and nitrogen-containing ordered mesoporous carbon-based catalysts for anion-exchange membrane fuel cell cathode, Electrochim. Acta 439 (2023), https://doi.org/10.1016/j.electacta.2022.141676.
[51] K. Kisand, A. Sarapuu, J.C. Douglin, A. Kikas, A. Treshchalov, M. Käärik, H. M. Piirsoo, P. Paiste, J. Aruväli, J. Leis, V. Kisand, A. Tamm, D.R. Dekel, K. Tammeveski, Templated nitrogen-, iron-, and cobalt-doped mesoporous nanocarbon derived from an alkylresorcinol mixture for anion-exchange membrane fuel cell application, ACS Catal. 12 (2022) 14050–14061, https://doi.org/10.1021/acscatal.2c03683.
[52] Y. Kumar, E. Kibena-Põldsepp, J. Kozlova, M. Rähn, A. Treshchalov, A. Kikas, V. Kisand, J. Aruväli, A. Tamm, J.C. Douglin, S.J. Folkman, I. Gelmetti, F. A. Garcés-Pineda, J.R. Galán-Mascarós, D.R. Dekel, K. Tammeveski, Bifunctional oxygen electrocatalysis on mixed metal phthalocyanine-modified carbon nanotubes prepared via pyrolysis, ACS Appl. Mater. Interfaces 13 (2021) 41507–41516, https://doi.org/10.1021/acsami.1c06737.
[53] Y. Kumar, E. Kibena-Põldsepp, M. Mooste, J. Kozlova, A. Kikas, J. Aruväli, M. Käärik, V. Kisand, J. Leis, A. Tamm, S. Holdcroft, J.H. Zagal, K. Tammeveski, Iron and nickel phthalocyanine-modified nanocarbon materials as cathode catalysts for anion-exchange membrane fuel cells and zinc-air batteries, SSRN Electron. J. (2022), https://doi.org/10.2139/ssrn.4049705.
[54] K. Kisand, A. Sarapuu, D. Danilian, A. Kikas, V. Kisand, M. Rähn, A. Treshchalov, M. Käärik, M. Merisalu, P. Paiste, J. Aruväli, J. Leis, V. Sammelselg, S. Holdcroft, K. Tammeveski, Transition metal-containing nitrogen-doped nanocarbon catalysts derived from 5-methylresorcinol for anion exchange membrane fuel cell application, J. Colloid Interface Sci. 584 (2021) 263–274, https://doi.org/10.1016/j.jcis.2020.09.114.
[55] M. Kodali, C. Santoro, S. Herrera, A. Serov, P. Atanassov, Bimetallic platinum group metal-free catalysts for high power generating microbial fuel cells, J. Power Sources 366 (2017) 18–26, https://doi.org/10.1016/j.jpowsour.2017.08.110.

[56] S. van den Brink, R. Kleijn, B. Sprecher, A. Tukker, Identifying supply risks by mapping the cobalt supply chain, Resour. Conserv. Recycl. 156 (2020), https://doi.org/10.1016/j.resconrec.2020.104743.
[57] M. Muhyuddin, A. Friedman, F. Poli, E. Petri, H. Honig, F. Basile, A. Fasolini, R. Lorenzi, E. Berretti, M. Bellini, A. Lavacchi, L. Elbaz, C. Santoro, F. Soavi, Lignin-derived bimetallic platinum group metal-free oxygen reduction reaction electrocatalysts for acid and alkaline fuel cells, J. Power Sources 556 (2023) 232416, https://doi.org/10.1016/j.jpowsour.2022.232416.
[58] M. Borghei, J. Lehtonen, L. Liu, O.J. Rojas, Advanced biomass-derived electrocatalysts for the oxygen reduction reaction, Adv. Mater. 30 (2018), https://doi.org/10.1002/adma.201703691.
[59] S. Das, S. Ghosh, T. Kuila, N.C. Murmu, A. Kundu, Biomass-derived advanced carbon-based electrocatalysts for oxygen reduction reaction 2 (2022) 155–177, https://doi.org/10.3390/biomass2030010.
[60] Q. Chen, X. Tan, Y. Liu, S. Liu, M. Li, Y. Gu, P. Zhang, S. Ye, Z. Yang, Y. Yang, Biomass-derived porous graphitic carbon materials for energy and environmental applications, J. Mater. Chem. A Mater. 8 (2020) 5773–5811, https://doi.org/10.1039/c9ta11618d.
[61] R. Chakraborty, K. V, M. Pradhan, A.K. Nayak, Recent advancement of biomass-derived porous carbon based materials for energy and environmental remediation applications, J. Mater. Chem. A Mater. (2022), https://doi.org/10.1039/d1ta10269a.
[62] L. Du, G. Zhang, X. Liu, A. Hassanpour, M. Dubois, A.C. Tavares, S. Sun, Biomass-derived nonprecious metal catalysts for oxygen reduction reaction: the demand-oriented engineering of active sites and structures, Carbon Energy 2 (2020) 561–581, https://doi.org/10.1002/cey2.73.
[63] J. Müller-Hülstede, D. Schonvogel, H. Schmies, P. Wagner, A. Dyck, M. Wark, Incorporation of activated biomasses in Fe-N-C catalysts for oxygen reduction reaction with enhanced stability in acidic media, ACS Appl. Energy Mater. 4 (2021) 6912–6922, https://doi.org/10.1021/acsaem.1c01018.
[64] M. Wang, S. Wang, H. Yang, W. Ku, S. Yang, Z. Liu, G. Lu, Carbon-based electrocatalysts derived from biomass for oxygen reduction reaction: a minireview, Front. Chem. 8 (2020), https://doi.org/10.3389/fchem.2020.00116.
[65] A. Lahiri, S. Daniel, R. Kanthapazham, R. Vanaraj, A. Thambidurai, L.S. Peter, A critical review on food waste management for the production of materials and biofuel, J. Hazard. Mater. Adv. 10 (2023) 100266, https://doi.org/10.1016/j.hazadv.2023.100266.
[66] J. Sherwood, The significance of biomass in a circular economy, Bioresour. Technol. 300 (2020), https://doi.org/10.1016/j.biortech.2020.122755.
[67] J.D. Hernández-Varela, D.I. Medina, Revalorization of coffee residues: advances in the development of eco-friendly biobased potential food packaging, Polymers 15 (2023) 2823, https://doi.org/10.3390/polym15132823.
[68] G.A. Figueroa Campos, J.P.H. Perez, I. Block, S.T. Sagu, P. Saravia Celis, A. Taubert, H.M. Rawel, Preparation of activated carbons from spent coffee grounds and coffee parchment and assessment of their adsorbent efficiency, Processes 9 (2021), https://doi.org/10.3390/pr9081396.
[69] S. Polat, P. Sayan, Assessment of the thermal pyrolysis characteristics and kinetic parameters of spent coffee waste: a TGA-MS study, energy sources, part A: recovery, Util. Environ. Eff. 45 (2023) 74–87, https://doi.org/10.1080/15567036.2020.1736693.
[70] M.C. Echeverria, M. Nuti, Valorisation of the residues of coffee agro-industry: perspectives and limitations, Open Waste Manag. J. 10 (2017) 13–22, https://doi.org/10.2174/1876400201710010013.
[71] Y.B. Andrade, J.K. Schneider, R.O. Farrapeira, A.N.L. Lucas, I.D.P. da Mota, T. R. Bjerk, L.C. Krause, E.B. Caramão, R. Hynek, Chromatographic analysis of N-compounds from the pyrolysis of spent coffee grounds, Sep. Sci. Plus. 6 (2023), https://doi.org/10.1002/sscp.202200057.
[72] S. Akula, A.K. Sahu, Heteroatoms co-doping (N, F) to the porous carbon derived from spent coffee grounds as an effective catalyst for oxygen reduction reaction in polymer electrolyte fuel cells, J. Electrochem. Soc. 166 (2019) F93–F101, https://doi.org/10.1149/2.0441902jes.
[73] S. Kabir, K. Artyushkova, A. Serov, P. Atanassov, Role of nitrogen moieties in N-doped 3D-graphene nanosheets for oxygen electroreduction in acidic and alkaline media, ACS Appl. Mater. Interfaces 10 (2018) 11623–11632, https://doi.org/10.1021/acsami.7b18651.
[74] A. Srinu, S.G. Peera, V. Parthiban, B. Bhuvaneshwari, A.K. Sahu, Heteroatom engineering and Co–doping of N and P to porous carbon derived from spent coffee grounds as an efficient electrocatalyst for oxygen reduction reactions in alkaline medium, ChemistrySelect 3 (2018) 690–702, https://doi.org/10.1002/slct.201702042.
[75] A. Ben Abdallah, A. Ben Hassen Trabelsi, M.V. Navarro, A. Veses, T. García, D. Mihoubi, Pyrolysis of tea and coffee wastes: effect of physicochemical properties on kinetic and thermodynamic characteristics, J. Therm. Anal. Calorim. 148 (2023) 2501–2515, https://doi.org/10.1007/s10973-022-11878-4.
[76] K. das Graças Souza, M.A. de Oliveira, G.U. Alcantara, G.M. Paulino, R.P. de Lima, O.E. Ferreira, A.C. da Silva Bezerra, L.P.S. Pimenta, A.R.T. Machado, Effect of pyrolysis temperature on the properties of the coffee grounds biochar and composition of its leachates, Chem. Pap. 77 (2023) 3947–3956, https://doi.org/10.1007/s11696-023-02755-x.
[77] K. Pandey, H.K. Jeong, Coffee waste-derived porous carbon for hydrogen and oxygen evolution reaction, Chem. Phys. Impact 6 (2023), https://doi.org/10.1016/j.chphi.2023.100175.
[78] D.Y. Chung, Y.J. Son, J.M. Yoo, J.S. Kang, C.Y. Ahn, S. Park, Y.E. Sung, Coffee waste-derived hierarchical porous carbon as a highly active and durable electrocatalyst for electrochemical energy applications, ACS Appl. Mater. Interfaces. 9 (2017) 41303–41313, https://doi.org/10.1021/acsami.7b13799.
[79] S.K. Ramasahayam, S. Azam, T. Viswanathan, Phosphorous, nitrogen co-doped carbon from spent coffee grounds for fuel cell applications, J. Appl. Polym. Sci. 132 (2015), https://doi.org/10.1002/app.41948.
[80] C. lo Vecchio, A.S. Aricò, V. Baglio, Application of low-cost Me-N-C (Me = Fe or Co) electrocatalysts derived from edta in direct methanol fuel cells (DMFCs), Materials 11 (2018), https://doi.org/10.3390/ma11071193.
[81] C. lo Vecchio, A.S. Aricò, G. Monforte, V. Baglio, EDTA-derived Co–N–C and Fe–N–C electro-catalysts for the oxygen reduction reaction in acid environment, Renew. Energy 120 (2018) 342–349, https://doi.org/10.1016/j.renene.2017.12.084.
[82] W. da Silva Freitas, B. Mecheri, C. Lo Vecchio, I. Gatto, V. Baglio, V.C.A. Ficca, A. Patra, E. Placidi, A. D'Epifanio, Metal-organic-framework-derived electrocatalysts for alkaline polymer electrolyte fuel cells, J. Power Sources 550 (2022), https://doi.org/10.1016/j.jpowsour.2022.232135.
[83] A. Carbone, R. Pedicini, I. Gatto, A. Saccà, A. Patti, G. Bella, M. Cordaro, Development of polymeric membranes based on quaternized polysulfones for AMFC applications, Polymers 12 (2020), https://doi.org/10.3390/polym12020283.
[84] C.Lo Vecchio, A. Carbone, S. Trocino, I. Gatto, A. Patti, V. Baglio, A.S. Aricò, Anionic exchange membrane for photo-electrolysis application, Polymers 12 (2020) 1–12, https://doi.org/10.3390/polym12122991.
[85] I. Gatto, A. Patti, A. Carbone, Assessment of the FAA3-50 polymer electrolyte for anion exchange membrane fuel cells, ChemElectroChem 10 (2023), https://doi.org/10.1002/celc.202201052.
[86] I. Gatto, A. Caprì, C. Lo Vecchio, S. Zignani, A. Patti, V. Baglio, Optimal operating conditions evaluation of an anion-exchange-membrane electrolyzer based on FUMASEP® FAA3-50 membrane, Int. J. Hydrog. Energy 48 (2023) 11914–11921, https://doi.org/10.1016/j.ijhydene.2022.04.176.
[87] A. Ferrari, J. Robertson, Interpretation of Raman spectra of disordered and amorphous carbon, Phys. Rev. B Condens. Matter. Mater. Phys. 61 (2000) 14095–14107, https://doi.org/10.1103/PhysRevB.61.14095.
[88] A. Sadezky, Raman microspectroscopy of soot and related carbonaceous materials: spectral analysis and structural information, Carbon 43 (2005) 1731–1742, https://doi.org/10.1016/j.carbon.2005.02.018.
[89] C. Guizani, K. Haddad, L. Limousy, M. Jeguirim, New insights on the structural evolution of biomass char upon pyrolysis as revealed by the Raman spectroscopy and elemental analysis, Carbon 119 (2017) 519–521, https://doi.org/10.1016/j.carbon.2017.04.078.
[90] R. Mercado, C. Wahl, J. En Lu, T. Zhang, B. Lu, P. Zhang, J.Q. Lu, A. Allen, J. Z. Zhang, S. Chen, Nitrogen-doped porous carbon cages for electrocatalytic reduction of oxygen: enhanced performance with iron and cobalt dual metal centers, ChemCatChem 12 (2020) 3230–3239, https://doi.org/10.1002/cctc.201902324.
[91] R. Gokhale, Y. Chen, A. Serov, K. Artyushkova, P. Atanassov, Direct synthesis of platinum group metal-free Fe-N-C catalyst for oxygen reduction reaction in alkaline media, Electrochem. Commun. (2016), https://doi.org/10.1016/j.elecom.2016.09.013.
[92] A. Serov, K. Artyushkova, N.I. Andersen, S. Stariha, P. Atanassov, Original mechanochemical synthesis of non-platinum group metals oxygen reduction reaction catalysts assisted by sacrificial support method, Electrochim. Acta 179 (2015) 154–160, https://doi.org/10.1016/j.electacta.2015.02.108.
[93] N. Bhuvanendran, S. Ravichandran, Q. Xu, T. Maiyalagan, H. Su, A quick guide to the assessment of key electrochemical performance indicators for the oxygen reduction reaction: a comprehensive review, Int. J. Hydrog. Energy 47 (2022) 7113–7138, https://doi.org/10.1016/j.ijhydene.2021.12.072.
[94] Y. Chen, R. Gokhale, A. Serov, K. Artyushkova, P. Atanassov, Novel highly active and selective Fe-N-C oxygen reduction electrocatalysts derived from *in-situ* polymerization pyrolysis, Nano Energy 38 (2017) 201–209, https://doi.org/10.1016/j.nanoen.2017.05.059.
[95] D. Testa, G. Zuccante, M. Muhyuddin, R. Landone, A. Scommegna, R. Lorenzi, M. Acciarri, E. Petri, F. Soavi, L. Poggini, L. Capozzoli, A. Lavacchi, N. Lamanna, A. Franzetti, L. Zoia, C. Santoro, Giving new life to waste cigarette butts: transformation into platinum group metal-free electrocatalysts for oxygen reduction reaction in acid, neutral and alkaline environment, Catalysts 13 (2023), https://doi.org/10.3390/catal13030635.
[96] A.N. Eledath, A. Edathiparambil Poulose, A. Muthukrishnan, Synthesis of few-layer graphene by ball-milling for oxygen reduction: kinetics and mechanistic insights, ACS Appl. Eng. Mater. (2023), https://doi.org/10.1021/acsaenm.3c00344.
[97] R. Nandan, H.R. Devi, R. Kumar, A.K. Singh, C. Srivastava, K.K. Nanda, Inner sphere electron transfer promotion on homogeneously dispersed Fe-N xcenters for energy-efficient oxygen reduction reaction, ACS Appl. Mater. Interfaces 12 (2020) 36026–36039, https://doi.org/10.1021/acsami.0c08086.
[98] Y. Jiang, L. Yang, T. Sun, J. Zhao, Z. Lyu, O. Zhuo, X. Wang, Q. Wu, J. Ma, Z. Hu, Significant contribution of intrinsic carbon defects to oxygen reduction activity, ACS Catal. 5 (2015) 6707–6712, https://doi.org/10.1021/acscatal.5b01835.
[99] X. Li, B.N. Popov, T. Kawahara, H. Yanagi, Non-precious metal catalysts synthesized from precursors of carbon, nitrogen, and transition metal for oxygen reduction in alkaline fuel cells, J. Power Sources 196 (2011) 1717–1722, https://doi.org/10.1016/j.jpowsour.2010.10.018.
[100] B. Ricciardi, B. Mecheri, W. da Silva Freitas, V.C.A. Ficca, E. Placidi, I. Gatto, A. Carbone, A. Capasso, A. D'Epifanio, Porous iron-nitrogen-carbon electrocatalysts for anion exchange membrane fuel cells (AEMFC), ChemElectroChem 10 (2023), https://doi.org/10.1002/celc.202201115.
[101] S. Wang, L. Zhang, Y. Qin, D. Ding, Y. Bu, F. Chu, Y. Kong, M. Liu, Co,N-codoped graphene as efficient electrocatalyst for hydrogen evolution reaction: insight into

the active centre, J. Power Sources 363 (2017) 260–268, https://doi.org/10.1016/j.jpowsour.2017.07.107.
[102] P. Teppor, R. Jäger, M. Paalo, A. Adamson, M. Härmas, O. Volobujeva, J. Aruväli, R. Palm, E. Lust, Peat as a carbon source for non-platinum group metal oxygen electrocatalysts and AEMFC cathodes, Int. J. Hydrog. Energy 47 (2022) 16908–16920, https://doi.org/10.1016/j.ijhydene.2022.03.199.
[103] V.M. Dhavale, S.K. Singh, A. Nadeema, S.S. Gaikwad, S. Kurungot, Nanocrystalline Fe-Fe2O3 particle-deposited N-doped graphene as an activity-modulated Pt-free electrocatalyst for oxygen reduction reaction, Nanoscale 7 (2015) 20117–20125, https://doi.org/10.1039/c5nr04929f.
[104] H.S. Kim, C.H. Lee, J.H. Jang, M.S. Kang, H. Jin, K.S. Lee, S.U. Lee, S.J. Yoo, W. C. Yoo, Single-atom oxygen reduction reaction electrocatalysts of Fe, Si, and N co-doped carbon with 3D interconnected mesoporosity, J. Mater. Chem. A Mater. 9 (2021) 4297–4309, https://doi.org/10.1039/d0ta11208a.
[105] C.Lo Vecchio, X. Lyu, I. Gatto, B. Zulevi, A. Serov, V. Baglio, Performance investigation of alkaline direct methanol fuel cell with commercial PGM-free cathodic materials, J. Power Sources 561 (2023), https://doi.org/10.1016/j.jpowsour.2023.232732.